

Magnetoelastic Effects in Doubly Clamped Electroplated $\text{Co}_{77}\text{Fe}_{23}$ Microbeam Resonators


M. Staruch,^{1,*} S.P. Bennett,¹ B.R. Matis,¹ J.W. Baldwin,¹ K. Bussmann,¹ D.B. Gopman,² Y. Kabanov,^{2,3} J.W. Lau,² R.D. Shull,² E. Langlois,⁴ C. Arrington,⁴ J. R. Pillars,⁴ and P. Finkel¹

¹*U.S. Naval Research Laboratory, Washington, D.C. 20375, USA*

²*Materials Science and Engineering Division, National Institute of Standards and Technology, Gaithersburg, Maryland 20899, USA*

³*Institute of Solid State Physics, Russian Academy of Science, Chernogolovka 142432, Russia*

⁴*Sandia National Laboratory, Albuquerque, New Mexico 87185, USA*

 (Received 4 January 2018; revised manuscript received 11 December 2018; published 12 March 2019)

Magnetostrictive $\text{Co}_{77}\text{Fe}_{23}$ films are fully suspended to produce free-standing, clamped-clamped, microbeam resonators. A negative or positive shift in the resonant frequency is observed for magnetic fields applied parallel or perpendicular to the length of the beam, respectively, confirming the magnetoelastic nature of the shift. Notably, the resonance shifts linearly with higher-bias fields oriented perpendicular to the beam's length. Domain imaging elucidates the distinction in the reversal processes along the easy and hard axes. Together, these results suggest that through modification of the magnetic anisotropy, the frequency shift and angular dependence can be tuned, producing highly magnetic-field-sensitive resonators.

DOI: [10.1103/PhysRevApplied.11.034028](https://doi.org/10.1103/PhysRevApplied.11.034028)

I. INTRODUCTION

There has been a surge of interest in low-power magnetoelastic (ME) magnetic-field sensors due to reports of high sensitivity with low-noise floors reaching several $\text{pT}/\sqrt{\text{Hz}}$ [1–5], comparable to fluxgate magnetometers. The basis of the ME sensor relies on the direct strain coupling of piezoelectric and magnetostrictive materials to achieve a magnetic-field- (H) induced change in the output voltage signal measured across the piezoelectric element. To overcome the $1/f$ noise and to simultaneously achieve high sensitivity over a large bandwidth at near-dc frequencies, several techniques have been used such as frequency conversion [6], modulation-demodulation [7,8], or a magnetically driven shift in the resonant frequency (f_0) [3,7,9–11]. To create a modulation in f_0 , magnetostrictive materials have previously been utilized that display a large change in the Young's modulus (E) induced by a changing magnetic field [12,13]. However, intrinsic and extrinsic stresses can negatively impact both this ΔE effect and the overall resultant magnetic-field sensitivity, which presents limitations on integrating these materials into real devices [14]. Alternately, the use of a magnetostriction-induced stress in a doubly clamped beam has recently been proposed while achieving a similar shift in f_0 with H [15–17]. By fixing both boundary conditions, as opposed to a cantilever structure, the intrinsic tension in the film

can be maintained along its length and in addition, magnetoelastic stresses will cause the resonance frequency to change with application of a magnetic field.

In this different geometry, controlling intrinsic resonator stress is an important consideration, and in particular, the total magnetic-anisotropy energy is critical to maximizing the magnetization rotation with an applied H , which results in the frequency shift for magnetostriction-based devices. Assuming a polycrystalline sample with zero average magnetocrystalline anisotropy and a constant exchange energy, the total free energy, F_{tot} , is defined by the Zeeman energy, shape anisotropy (demagnetization energy), and contributions from intrinsic or extrinsic stresses due to magnetoelastic effects, which is expressed as

$$F_{\text{tot}} = F_{\text{Zeeman}} + F_{\text{shape}} + F_{\text{magnetoelastic}}. \quad (1)$$

Adopting the expression for the shape energy anisotropy of a rectangular prism [18], the total magnetic free energy density can be written as

$$\begin{aligned} F_{\text{tot}} = & -HM[\cos\theta\cos\theta_H + \sin\theta\sin\theta_H\cos(\phi - \phi_H)] \\ & + \frac{1}{2}(N_z - N_x)M^2\cos^2\theta \\ & + \frac{1}{2}(N_y - N_x)M^2\sin^2\theta\sin^2\phi - \frac{3}{2}\lambda_s\sigma_i\sin^2\phi, \end{aligned} \quad (2)$$

*margo.staruch@nrl.navy.mil

where σ_i is the intrinsic stress assumed to be in the plane of the resonator, M is the magnetization, λ_s is the saturation magnetostriction, (θ, ϕ) and (θ_H, ϕ_H) are the angles for magnetization and applied field in spherical coordinates, respectively, and N_x , N_y , and N_z are the diagonal components ($N_{ii} = N_i$) of the demagnetization tensor N_{ji} along the long edge (x), short edge (y), and normal direction (z). Minimization of F_{tot} will determine the initial magnetization direction and consequently the rotation of the magnetic moment with applied field. The magnetization direction determines the magnitude of the magnetostrictive-induced stresses, and therefore, the change in f_0 . To develop the highest magnetostrictive stress, a 90° magnetization rotation is optimal (perpendicular to the beam length, in the plane of the film). It is also important to note that the minimization of this energy becomes more of a problem when the magnetic material has a more complex pattern than simply rectangular, and can give rise to interesting magnetization dynamics.

We previously reported measurements of a frequency shift in a clamped-clamped beam with H applied perpendicular to the length of the beam [16,17]. In this work, we use a facile electrodeposition route at near-room temperature to increase the thickness of the magnetic layer as well as significantly reduce the fabrication-introduced intrinsic stresses in the film before substrate release. The goal is to modify the magnetic anisotropy and examine the effects on the frequency tunability.

II. EXPERIMENTAL DETAILS

Cobalt-iron electrodeposition is completed using a sulfamate chemistry and pulsed-plating parameters developed at Sandia National Laboratories. For microbeam fabrication, $5.2 \mu\text{m}$ of polycrystalline $\text{Co}_{77}\text{Fe}_{23}$ is deposited on low-pressure chemical vapor deposited (LPCVD) Si_3N_4 films on Si using standard photolithography patterning with beam dimensions of 1 mm in length and $40 \mu\text{m}$ in width [see Fig. S1 in the Supplemental Material [19]]. The silicon substrate is etched away from the back of the microbeams using an 80°C KOH immersion for 3.5 h. Before immersion, a backside wafer patterning and CF_4 plasma reactive ion etch (RIE) is used to pattern a 100-nm plasma-enhanced CVD SiN hard mask, while the front side is coated with a ProTek (Brewer Science, Rolla, MO) barrier coating to prevent etching of the $\text{Co}_{77}\text{Fe}_{23}$ beams. To directly measure the magnetostriction coefficient (λ_s) of our films, bimorph cantilevers of $\text{Co}_{77}\text{Fe}_{23}$ are deposited on flexible copper substrates for the laser Doppler vibrometer (LDV) and capacitance gauge measurements [20] [see Fig. S2(a) in the Supplemental Material [19]]. For all of our films, the magnetostriction saturated for applied magnetic fields in excess of 100 mT, which is consistent with the field at which saturation magnetization is achieved according to measurements made with a vibrating-sample

magnetometer for a $5 \times 5 \text{ mm}^2$ sample. Values of λ_s up to 80 ppm are found for the $\text{Co}_{77}\text{Fe}_{23}$ films that are within the range observed for high-quality sputtered films [21–23], confirming the comparable quality of electrodeposited samples.

Mechanical measurements, including measurements of magnetostriction and f_0 , are carried out using a LDV and utilizing a lock-in technique. Magnetization measurements are performed with a vibrating sample magnetometer. We also employ a magneto-optic indicator film (MOIF) technique to observe magnetic domain walls [24–26]. The indicator film's in-plane magnetization can be locally rotated out of the plane by magnetic stray fields exiting the $\text{Co}_{77}\text{Fe}_{23}$ beam sample (at domain walls, ripples, or sample edges), and incident light on the indicator film experiences a large magneto-optic Faraday rotation. From the polarization contrast at these locations, an image of domain walls in the beams is generated.

III. RESULTS

Figure 1 shows the measured resonator amplitude as a function of frequency utilizing an external piezoelectric actuator for one of the resonators. With increasing drive amplitude, we observe nonlinear Duffing behavior, which manifests as an asymmetric distortion of the resonance peak as shown in Fig. 1(a). The peak intensity and line-shape are also found to be dependent upon the direction of the frequency sweep, as shown in Fig. 1(b). Such nonlinear, bipolar behavior has previously been proposed as a two-state bit memory by shifting the frequency through the application of a magnetic field [27].

At low-drive amplitude (0.2 V to the piezo stack) where a nondistorted Lorentzian peak shape is observed, f_0 is measured with a magnetic bias field applied in the plane of the film, both perpendicular (H_\perp) and parallel (H_\parallel) to the long axis of the resonator, and the results are shown in Figs. 2(a) and 2(b), respectively. For H_\perp , a shift in f_0 is observed above 20–30 mT. Interestingly, no saturation in the frequency shift for this field-sweep direction is observed at fields as high as 300 mT (the limit of the magnet). This is in stark contrast to the frequency shift data for the H_\parallel data set [Fig. 2(b)], which shows an almost complete saturation of the magnetization above approximately 100 mT (this correlates with the magnetostriction data [see Fig. S2(a) in the Supplemental Material [19]] that show saturation around this field as well. This discrepancy is most likely a direct result of a hard magnetization axis in the direction perpendicular to the length of the resonator, consistent with the demagnetizing energy (large N_y, N_z) induced by the high aspect ratio of the beams.

One possible reason for the observed behavior is that the nonsaturation of the magnetization along the hard axis results from the large energy barrier for magnetization rotation. The saturation of the magnetization will directly

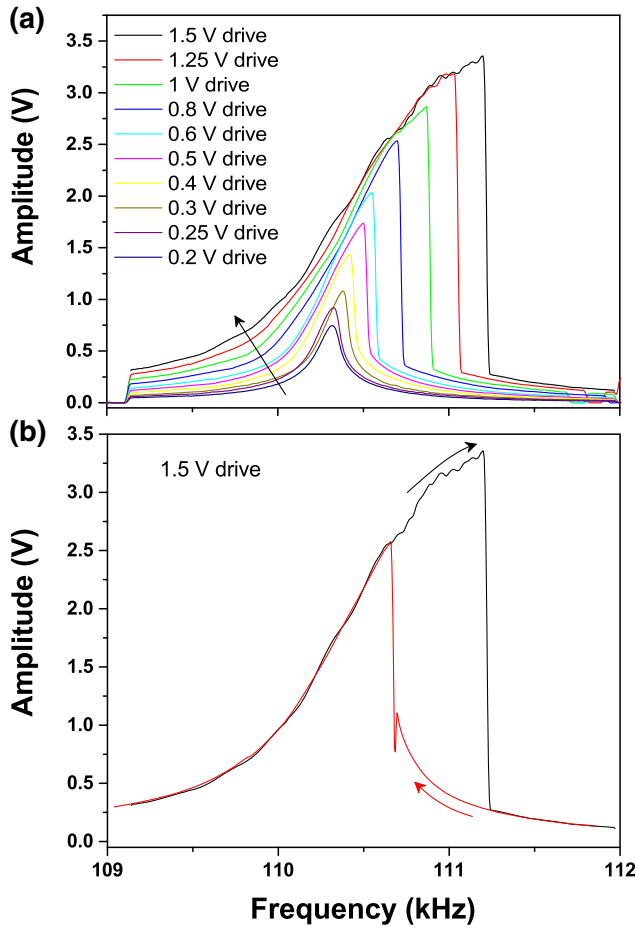


FIG. 1. Resonant amplitude vs frequency (a) for different piezoelectric-drive amplitudes and (b) showing nonlinear oscillator behavior with a hysteresis between up and down sweeps for highest drive amplitude given in (a).

correlate to the saturation of the magnetostriction in the beam, and as long as the magnetization is rotating, a magnetostrictive effect will still be observed. We confirm this for the present $\text{Co}_{77}\text{Fe}_{23}$ beams and the data is shown in Fig. 3. Magnetization measurements of a single beam cleaved from the sample show clear easy-axis behavior for H_{\parallel} , while for H_{\perp} , the hysteresis loop is consistent with a magnetically hard axis. This is further compared with the hysteresis loops for a square sample grown on the same wafer as the beam, which show isotropic in-plane behavior [see Fig. S2(b) in the Supplemental Material [19]] and confirms that the observed hard axis is resultant from the anisotropy (both shape and stress) for the beam. It is also possible that for H_{\perp} , a large magnetic torque $\tau = mB \sin \theta$ (where m is the magnetic moment) is generated due to the magnetization being primarily aligned parallel to the length of the beam. Torque effects should also give rise to a linear increase in frequency with field, and a torsional resonance mode has previously been shown to dominate the fundamental bending mode depending on the

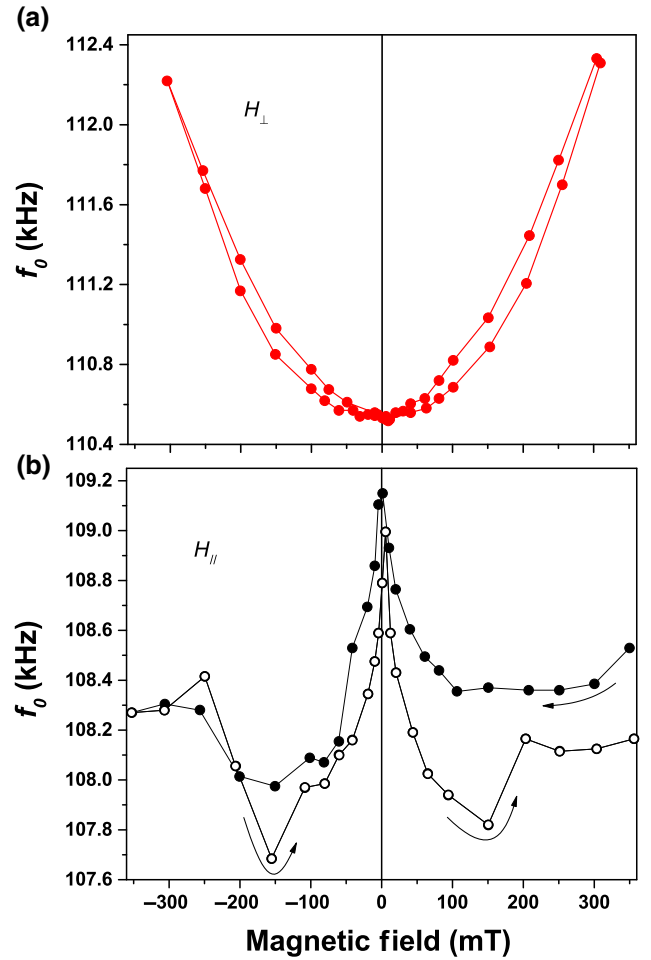


FIG. 2. Resonant frequency f_0 vs applied magnetic field $\mu_0 H$ for (a) field applied in-plane and perpendicular to the long axis of the beam (parallel to short axis) and (b) field applied in-plane, parallel to the long axis of the beam. The field-sweep direction is indicated by arrows.

magnetic-anisotropy angle with respect to H [28]. Future measurements at fields near or above the saturation field of $\mu_0 H \sim 1.35$ T can be used to decouple the contributions from these two mechanisms.

The opposite signs for the frequency shift in the parallel and perpendicular directions (Fig. 2) are consistent with the development of magnetostrictive stress: for a field applied along the beam, a tensile magnetoelastic stress is expected to develop, whereas a compressive stress will develop for field applied perpendicular to the beam due to the corresponding rotation of the magnetic moments. Notably though, there are two sharp peaks in f_0 vs H that occur when H_{\parallel} is near the coercive field (H_C). In contrast to the H_{\perp} data set, the frequency response for H_{\parallel} also appears to saturate above 150 mT except for two additional anomalies observed for when the magnetic field is swept from negative to positive (increasing branch) just before saturation. Another interesting feature to note is

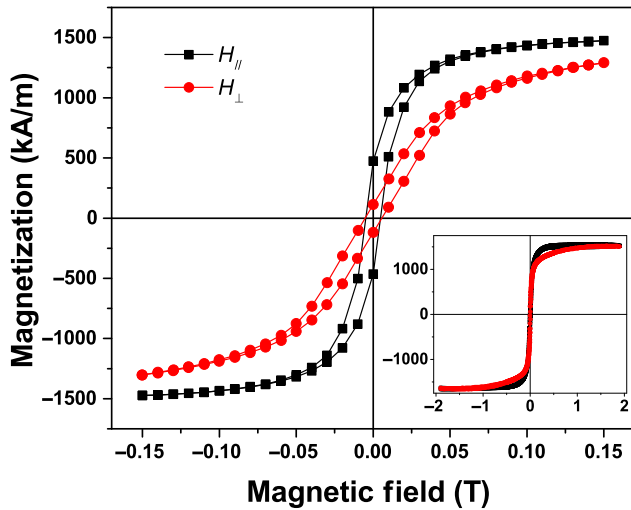


FIG. 3. Magnetization vs applied magnetic field for H applied along the long axis and short axis of a single $\text{Co}_{77}\text{Fe}_{23}$ microbeam. The inset shows the full-scale magnetic hysteresis loop.

that above this 150-mT field, the peak shape goes from Lorentzian to distorted non-Lorentzian even though the drive voltage is kept constant (see Fig. S3 in the Supplemental Material [19]). This occurs starting at the inflection point in the f_0 vs H_{\parallel} plot and above saturation of the magnetization and magnetostriction. This phenomenon is not yet fully understood, but the distorted shape of the resonance peak is highly indicative of nonlinearity arising in the beam. It is also of interest to note that the beam should be nominally saturated at 100 mT for H_{\parallel} (which does correspond to saturation of f_0 observed in the down sweep). One possibility is that this could be due to a slight misalignment of the beam in the field. Any effects from this may also be amplified if the magnetization is not fully rotated by 180° by the applied negative field, which would explain the difference regarding the down- and up-field sweeps.

The value of magnetic-field sensitivity, defined as df_0/dH , is plotted in Fig. 4 for both fields applied parallel and perpendicular to the beam's length. For H_{\parallel} , two large peaks occur at roughly $\pm H_C$, reaching a maximum df_0/dH of 40 Hz/mT. This corresponds to 0.03% f_0 /mT, which is comparable or slightly higher than values observed for other proposed sensors where magnetostriction dominates [15,29], but is lower than previously observed df_0/dH values for cantilever beams utilizing the ΔE effect [3,11]. However, while df_0/dH is low at smaller magnetic fields for H_{\perp} , the value grows linearly with increasing field, and while the value of field sensitivity may decrease as the material approaches saturation, it is not expected to saturate until well over a 1-T applied field (based on the magnetization curves).

MOIF microscopy is used to study the domain formation and dynamics of the $\text{Co}_{77}\text{Fe}_{23}$ microbeams for H_{\parallel}

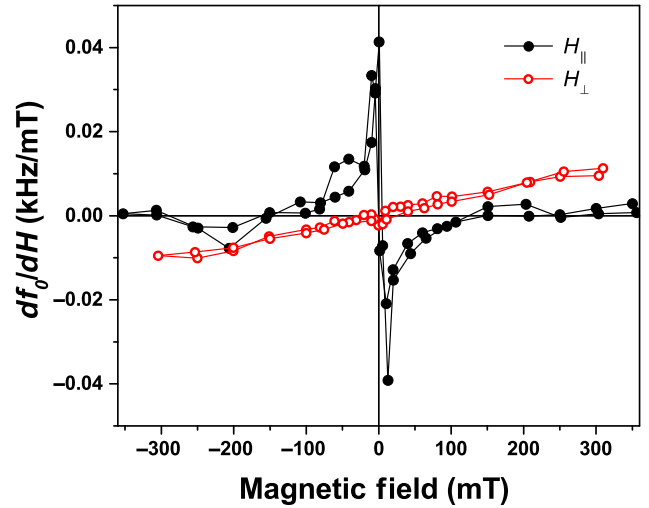


FIG. 4. The derivative of the field-dependent frequency data, or the magnetic-field sensitivity, vs applied magnetic field.

and H_{\perp} to better understand the remagnetization processes underlying the spectral response of the $\text{Co}_{77}\text{Fe}_{23}$ -based magnetic-field sensors. In Figs. 5(a)–5(c), simultaneous MOIF imaging of two $\text{Co}_{77}\text{Fe}_{23}$ microbeams are shown under a series of representative magnetic fields applied along the parallel direction (x direction). MOIF microscopy videos covering the entire remagnetization behavior under easy-axis and hard-axis fields are included as Supplemental Material [19]. After applying a moderate positive field along the x axis (6.9 mT), the magnetic field is reduced by half in (a) (3.5 mT), for which the magnetization remains aligned with the positive field direction. After applying a small reversed field in (b) of -1.4 mT, we notice that the rectangular termination pads of the beams are first to nucleate reversed domains, shown by the change from light-to-dark (dark-to-light) contrast along the perimeter of the left (right) termination pads. Increasing the reversed field to -3.4 mT in (c), we find that the termination pads are predominantly remagnetized, while the beam remains magnetized along the positive direction. The beam magnetization direction in (c) is evident from the MOIF contrast along the beam axis, specifically where the dark-to-gray transition and the gray-to-bright transitions indicate that the magnetization within the gray region is uniform and opposite the reversed magnetization in the termination pads. Interestingly, the diffuse and extensive bright- and dark-contrast regions entering into the beams indicate incoherent magnetization configurations through the thickness. This behavior indicates that beams of this thickness cannot be considered entirely within a planar-remagnetization model for fields applied along the easy axis. In order to gain better insight into the magnetization configuration of the beams along the easy axis, a single beam is taken from these samples and is thinned by ion bombardment to electron transparency. Lorentz

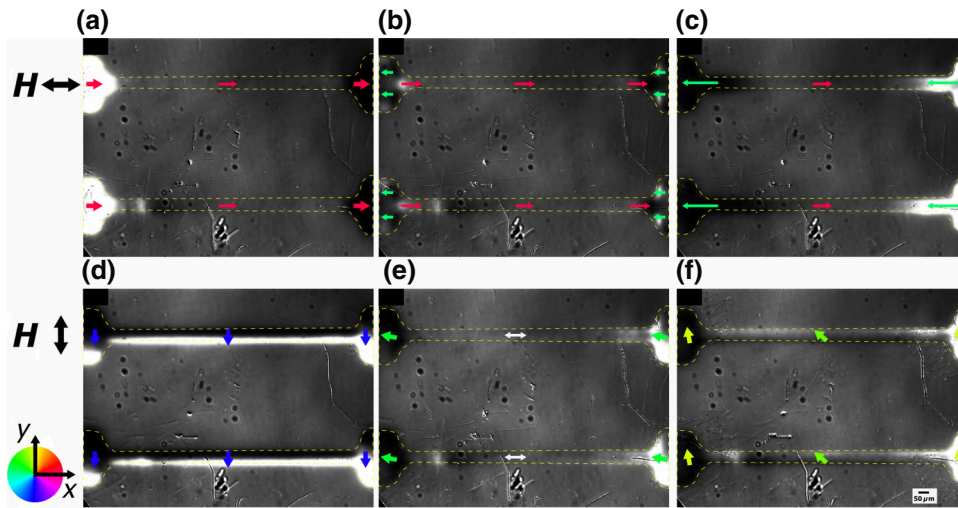


FIG. 5. MOIF domain images of two $\text{Co}_{77}\text{Fe}_{23}$ microbeams. An external magnetic field is applied along the beam long axis: (a) +3.5 mT, (b) -1.4 mT, and (c) -3.8 mT; or the beam short axis: (d) -6.9 mT, (e) 0.3 mT, and (f) +1.4 mT. The color wheel indicates the direction of magnetization; the white arrows represent a region where the MOIF contrast is insufficient to determine direction.

Transmission Electron Microscopy (see Fig. S4 in the Supplemental Material [19]) reveals a longitudinal magnetization ripple along the easy axis, which is indicative of polycrystalline grains with random deviations of orientation, composition, and strain in the individual crystallites. We also can see the narrow domain walls, which were otherwise below the resolution of the MOIF technique.

Figures 5(d)–5(f) illustrate the short-axis reversal behavior of the beams. Starting at a moderate negative field (-6.9 mT) along the y axis, Fig. 5(d) shows strong contrast from the top and bottom edges of the beam and contact pads indicate that the magnetization is primarily aligned with the applied field. As the field is reversed to 0.3 mT in Fig. 5(e), the contrast at the edges of the beam has mostly disappeared, corresponding to the magnetization rotating back onto the easy axis at small fields. A large contrast at the termination pads shows that the magnetization has largely changed sign, indicating reversal has already been initiated in the pads. Under increasing fields, the magnetization in the beams can ultimately overcome the anisotropy of the structure and rotate onto the short axis. The beginnings of such rotation can be seen in Fig. 5(f) at 1.4 mT.

We can also better interpret the magnetic hysteresis loops in Fig. 3 in light of the magneto-optic images. The rectangular termination pads reverse by domain-wall propagation and generate the largest contribution to the observed hysteresis in the magnetization curves. This is evident in both the easy-axis and the hard-axis hysteresis loops as the pads are only weakly influenced by the shape anisotropy of the beams. The beams themselves have virtually zero hysteresis (Figs. 5(e) and 5(f) and microscopy videos in the Supplemental Material) for fields applied along the hard axis, a result we could not have otherwise determined from the magnetization curves due to the large signal from the pads. This highlights the extent to which the fabrication of magnetic

microdevices with complex patterns will strongly affect the local magnetic properties, and therefore, complicate analysis of these structures with bulk measurement techniques. We also note that remagnetization begins with the termination pads before advancing into the beams, either by domain-wall propagation [Figs. 5(b) and 5(c)] for easy-axis fields, or rotation [Figs. 5(d)–5(f)] under hard-axis fields.

IV. DISCUSSION

A comparison of the figure of merit df_0/dH and the equivalent magnetic noise floor for several ME sensors in the literature is shown in Table I. It can be observed that df_0/dH , which is theoretically directly related to the equivalent magnetic noise [16], may vary for similar materials. However, even for less than ideal values of frequency shift (less than 1% shift in f_0), noise floors in the hundreds of $\text{pT}/\sqrt{\text{Hz}}$ can be observed (with some inconsistencies given different electronic detection schemes with variable electronic-noise contributions). This work has focused on both the contributions for parallel vs perpendicular applied fields, which has not previously been presented for similar systems. It is in this way that we see that although the magnetic field sensitivity is lower for H_{\perp} , it is maximized at very-high-bias magnetic fields compared to ΔE sensors with a very narrow working point. Based on our values of df_0/dH and comparing to those in Table I, we would expect to have very good sensitivity at these high biases. This large nonsaturating magnetic-field sensitivity for H_{\perp} as shown in Fig. 4 makes the present doubly clamped $\text{Co}_{77}\text{Fe}_{23}$ resonators very promising candidates for highly sensitive magnetic-field detection in a high-bias field, which would be extremely useful for use in nuclear magnetic resonance (NMR) or magnetic resonance imaging (MRI) systems [30].

TABLE I. The figure of merit df_0/dH and working point for several ME sensors, and the resultant equivalent magnetic noise floor.

Magnetic phase	df_0/dH ($\%f_0/\text{mT}$)	Working point (mT)	Equivalent magnetic noise ($\text{pT}\sqrt{\text{Hz}}$)	Ref.
Fe-Ga-B	0.6	0.5 (H_{\parallel})	300	[3]
(Fe ₉₀ Co ₁₀) ₇₈ Si ₁₂ B ₁₀	1.5	2 (H_{\parallel})	12 000	[11]
Fe-Co-Si-B	—	0.65 (H_{\parallel})	7.1	[6]
Bulk Metglas	8	0.5 (H_{\parallel})	5	[1,14]
Fe-Ga-B	1.44	1.2 (H_{\parallel})	800	[30]
Fe-Co-Si-B/Cr multilayer	0.97	0.7 (H_{\parallel})	140	[7]
Co ₆₈ Fe ₃₂	0.007	30–50 (H_{\perp})	100	[16]
Co ₇₇ Fe ₂₃	0.03	6.6 (H_{\parallel})	—	This work
	0.009	>300 (H_{\perp})		

V. CONCLUSIONS

In summary, free-standing beams with clamped-clamped boundary conditions are fabricated using a combination of electrodeposition, photolithography, and high-temperature wet etching. In testing, a clear nonlinear behavior is observed while driving the beams with a piezoelectric actuator at resonance. The resonant frequency shifts with application of a magnetic field due to the development of a magnetoelastic strain along the length of the structure. With a magnetic field applied along the length of the structure, easy-axis behavior is observed in the magnetization and reversal is achieved through domain nucleation and propagation, whereas fields along the short (hard) axis display coherent rotation of the magnetization within domains. The individual contributions of the pads and the beams to the hysteretic behavior is revealed through domain imaging. Along the hard axis, the large field required for saturation matches with the linear behavior observed at higher fields in the magnetic field sensitivity df_0/dH . This highly anisotropic clamped-clamped cantilever structure results in a nonsaturation of frequency shift with magnetic fields of over 300 mT applied perpendicular to the length of the beam, making such a microstructure a prime candidate for magnetic-field sensing with a vastly increased operational range.

ACKNOWLEDGMENTS

The work at NRL was supported by the Office of Naval Research (ONR) through the Naval Research Laboratory's Basic Research Program.

- [1] Y. Wang, D. Gray, D. Berry, J. Gao, M. Li, J. Li, and D. Viehland, An extremely low equivalent magnetic noise magnetoelectric sensor, *Adv. Mater.* **23**, 4111 (2011).
- [2] S. Marauska, R. Jahns, H. Greve, E. Quandt, R. Knöchel, and B. Wagner, MEMS magnetic field sensor based on magnetoelectric composites, *J. Micromech. Microeng.* **22**, 065024 (2012).

- [3] T. Nan, Y. Hui, M. Rinaldi, and N. X. Sun, Self-biased 215 MHz magnetoelectric NEMS resonator for ultra-sensitive DC magnetic field detection, *Sci. Rep.* **3**, 1985 (2013).
- [4] P. Finkel, S. E. Lofland, and E. Garrity, Magnetoelastic/piezoelectric laminated structures for tunable remote contactless magnetic sensing and energy harvesting, *Appl. Phys. Lett.* **94**, 10 (2009).
- [5] S. Zabel, J. Reermann, S. Fichtner, C. Kirchhof, E. Quandt, B. Wagner, G. Schmidt, and F. Faupel, Multimode delta-E effect magnetic field sensors with adapted electrodes, *Appl. Phys. Lett.* **108**, 222401 (2016).
- [6] R. Jahns, H. Greve, E. Woltermann, E. Quandt, and R. Knöchel, Sensitivity enhancement of magnetoelectric sensors through frequency-conversion, *Sens. Actuators A Phys.* **183**, 16 (2012).
- [7] S. Zabel, C. Kirchhof, E. Yazar, D. Meyners, E. Quandt, and F. Faupel, Phase modulated magnetoelectric delta-E effect sensor for sub-nano tesla magnetic fields, *Appl. Phys. Lett.* **107**, 152402 (2015).
- [8] X. Zhuang, M. L. C. Sing, C. Dolabdjian, P. Finkel, J. Li, and D. Viehland, Theoretical intrinsic equivalent magnetic noise evaluation for magneto (elasto) electric sensors using modulation techniques, *IEEE Sens. J.* **14**, 150 (2014).
- [9] A. Kittmann, P. Durdaut, S. Zabel, J. Reermann, J. Schmalz, B. Spetzler, D. Meyners, N. X. Sun, J. McCord, M. Gerken, G. Schmidt, M. Höft, R. Knöchel, F. Faupel, and E. Quandt, Wide band low noise love wave magnetic field sensor system, *Sci. Rep.* **8**, 278 (2018).
- [10] B. Gojdka, R. Jahns, K. Meurisch, H. Greve, R. Adelung, E. Quandt, R. Knöchel, and F. Faupel, Fully integrable magnetic field sensor based on delta-E effect, *Appl. Phys. Lett.* **99**, 223502 (2011).
- [11] R. Jahns, S. Zabel, S. Marauska, B. Gojdka, B. Wagner, R. Knöchel, R. Adelung, and F. Faupel, Microelectromechanical magnetic field sensor based on ΔE effect, *Appl. Phys. Lett.* **105**, 052414 (2014).
- [12] A. M. Severino and F. P. Missell, New analysis of the small-angle-magnetization-rotation method for magnetostriction measurements on amorphous ribbons, *J. Magn. Magn. Mater.* **68**, 291 (1987).
- [13] D. Y. Kim, C. G. Kim, H. C. Kim, and U. H. Sung, Stress dependence of ΔE in amorphous ribbon, *J. Appl. Phys.* **81**, 5811 (1997).
- [14] M. Staruch, M.-T. Yang, J. F. Li, C. Dolabdjian, D. Viehland, and P. Finkel, Frequency reconfigurable phase

- modulated magnetoelectric sensors using ΔE effect, *Appl. Phys. Lett.* **111**, 032905 (2017).
- [15] J. Kiser, P. Finkel, J. Gao, C. Dolabdjian, J. Li, and D. Viehland, Stress reconfigurable tunable magnetoelectric resonators as magnetic sensors, *Appl. Phys. Lett.* **102**, 042909 (2013).
- [16] J. Kiser, R. Lacombe, K. Bussmann, C. J. Hawley, J. E. Spanier, X. Zhuang, C. Dolabdjian, S. Lofland, and P. Finkel, Magnetostrictive stress reconfigurable thin film resonators for near direct current magnetoelectric sensors, *Appl. Phys. Lett.* **104**, 072408 (2014).
- [17] M. Staruch, C. Kassner, S. Fackler, I. Takeuchi, K. Bussmann, S. E. Lofland, C. Dolabdjian, R. Lacombe, and P. Finkel, Effects of magnetic field and pressure in magnetoelastic stress reconfigurable thin film resonators, *Appl. Phys. Lett.* **107**, 032909 (2015).
- [18] Y. Zhai, J. Shi, X. Y. Zhang, L. Shi, Y. X. Xu, H. B. Huang, Z. H. Lu, and H. R. Zhai, A study of the non-uniform effect on the shape anisotropy in patterned NiFe films of ferromagnetic resonance, *J. Phys. Condens. Matter* **14**, 7865 (2002).
- [19] See Supplemental Material at <http://link.aps.org/supplemental/10.1103/PhysRevApplied.11.034028> for general film properties, resonance data, and additional domain imaging.
- [20] E. du Trémolet de Lacheisserie and J. C. Peuzin, Magnetostriction and internal stresses in thin films: the cantilever method revisited, *J. Magn. Magn. Mater.* **152**, 231 (1996).
- [21] D. Hunter, W. Osborn, K. Wang, N. Kazantseva, J. Hattrick-Simpers, R. Suchoski, R. Takahashi, M. L. Young, A. Mehta, L. A. Bendersky, S. E. Lofland, M. Wuttig, and I. Takeuchi, Giant magnetostriction in annealed $\text{Co}_{1-x}\text{Fe}_x$ thin-films, *Nat. Commun.* **2**, 518 (2011).
- [22] H. S. Jung, W. D. Doyle, and S. Matsunuma, Influence of underlayers on the soft properties of high magnetization FeCo films, *J. Appl. Phys.* **93**, 6462 (2003).
- [23] M. D. Cooke, L.-C. Wang, R. Watts, R. Zuberek, G. Heydon, W. M. Rainforth, and G. A. Gehring, The effect of thermal treatment, composition and substrate on the texture and magnetic properties of FeCo thin films, *J. Phys. D: Appl. Phys.* **33**, 1450 (2000).
- [24] V. S. Gornakov, Y. P. Kabanov, V. I. Nikitenko, O. A. Tikhomirov, A. J. Shapiro, and R. D. Shull, Chirality of a forming spin spring and remagnetization features of a bilayer ferromagnetic system, *J. Exp. Theor. Phys.* **99**, 602 (2004).
- [25] I. Gilbert, P. J. Chen, D. B. Gopman, A. L. Balk, D. T. Pierce, M. D. Stiles, and J. Unguris, Nanoscale imaging of magnetization reversal driven by spin-orbit torque, *Phys. Rev. B* **94**, 094429 (2016).
- [26] M. Staruch, D. B. Gopman, Y. L. Iunin, R. D. Shull, S. F. Cheng, K. Bussmann, and P. Finkel, Reversible strain control of magnetic anisotropy in magnetoelectric heterostructures at room temperature, *Sci. Rep.* **6**, 37429 (2016).
- [27] T. Onuta, Y. Wang, S. E. Lofland, and I. Takeuchi, Multi-ferroic operation of dynamic memory based on heterostructured cantilevers, *Adv. Mater.* **27**, 202 (2015).
- [28] A. Garnier, T. Bourouina, H. Fujita, T. Hiramoto, E. Orsier, and J.-C. Peuzin, Magnetic actuation of bending and torsional vibrations for 2D optical-scanner application, *Sens. Actuators A Phys.* **84**, 156 (2000).
- [29] H. Lin, T. Nan, Zhenyun Qian, Y. Gao, Y. Hui, X. Wang, R. Guo, A. Belkessam, Wei Shi, M. Rinaldi, and N. X. Sun, Tunable RF band-pass filters based on NEMS magnetoelectric resonators, in 2016 IEEE MTT-S Int. Microw. Symp. (IEEE, 2016), pp. 1–4.
- [30] M. Li, A. Matyushov, C. Dong, H. Chen, H. Lin, T. Nan, Z. Qian, M. Rinaldi, Y. Lin, and N. X. Sun, Ultra-sensitive NEMS magnetoelectric sensor for picotesla DC magnetic field detection, *Appl. Phys. Lett.* **110**, 143510 (2017).